THE JOURNAL OF PHYSICAL CHEMISTRY C
A JOURNAL OF THE AMERICAN CHEMICAL SOCIETY

Ethylene Dimerization on Ni-Supported NU-1000: A Comprehensive Theoretical Study

Thanh-Nam Huynh,[‖] Nikita A. Matsokin,[‖] Felix Studt, Karin Fink,* and Dmitry I. Sharapa*

Cite This: J. Phys. Chem. C 2025, 129, 22377−22389

Read Online

ACCESS | Metrics & More | Article Recommendations | Supporting Information

ABSTRACT: Single-atom catalysts supported on metal−organic frameworks have attracted growing attention over the past few decades, as have theoretical studies on these systems. While accurate predictions are highly desirable for improved mechanistic understanding and catalyst design, benchmarks on methodologies employed for such systems remain limited. In this work, we present a comprehensive evaluation of computational models and various density functionals for catalytic ethylene dimerization on a Ni single-atom catalyst supported on NU-1000. We elucidate the nature of the mononuclear Ni sites and their catalytic transformations along the reaction pathway via the Cossee-Arlman mechanism. We assess the adequacy of truncated cluster models and the accuracy of different density functionals by comparing them with the highly accurate yet computationally demanding periodic model and the DLPNO−CCSD(T) method, respectively.

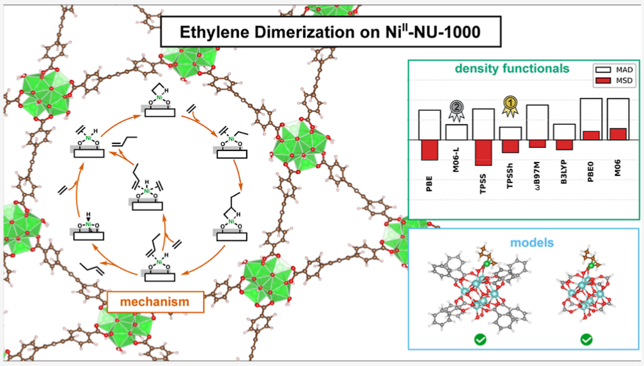

1. INTRODUCTION

In the past decades, metal−organic frameworks (MOFs) have drawn considerable attention in a wide variety of applications, especially in heterogeneous catalysis as catalysts per se or solid supports for single active catalysts.[1,2] The class of materials has shown promising potential in bridging the gap between homogeneous and heterogeneous catalysts because of its well-defined crystalline and highly porous structures and versatile amenability to structural modifications. This is realized by integrating the catalytic environment of well-known homogeneous catalysts to either the metal nodes (i.e., secondary building units) or organic linkers of the MOFs.

The oligomerization process plays a vital role as it converts abundant ethylene, for example from shale gas or methanol-to-olefins processes, into linear α-olefins (LAO), which are important ingredients for the production of plastics, surfactants, lubricants, and also aviation fuels.[3−6] Recently, increasing efforts have been made to utilize single-atom catalysts (SACs) supported on MOFs for selective ethylene oligomerization reactions.[7−11] The zirconia-based MOFs, such as NU-1000[12] and UiO-66,[13] are reportedly among the most popular supports for ethylene oligomerization catalysts due to their high thermal and chemical stability as well as catalytic performance.[14,15] Their popularity has been demonstrated in a rising number of experimental and theoretical studies.[10,11,14−22] Computational methods have shown their usefulness not only in shedding light on the mechanisms of the reactions but also in guiding experimental explorations, given the vast structural tunability of the materials. However, the complex and extended structures of SACs in MOFs, which consist of inorganic nodes, organic linkers, and incorporated active sites, pose a great deal of technical challenges in the modeling of such materials.

The first challenge is to choose a meaningful representation of the catalytic system. An appropriate computational model should include the accurate chemical environment of the catalytically active site as well as the confined steric environment within a pore at which the active site resides. Meanwhile, the computational cost should also be considered when choosing a model. Regarding this, cluster models, which account for partial or none of linkers' steric effects, are more commonly used to explore catalytic mechanisms, as compared to periodic models, which are often employed to examine the framework's properties. Bernales and co-workers provided an early theoretical elucidation of the mechanisms of ethylene dimerization reactions over so-called Ni-AIM-NU-1000 and Co-AIM-NU-1000 catalysts.[11] In this study, DFT calculations were performed on a formate cluster model (where linkers were represented by formate groups). Based on these calculations, the authors concluded that the Cossee-Arlmann pathway (linear insertion, Scheme 1) was the energetically favorable mechanism. Later, Ye and colleagues[16] employed

Received: August 26, 2025
Revised: October 27, 2025
Accepted: November 11, 2025
Published: November 21, 2025

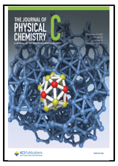

Scheme 1. Schematic Illustration of the Cossee-Arlman Mechanism for the Ethylene Dimerization Reaction on Ni^{II}−NU-1000[a]

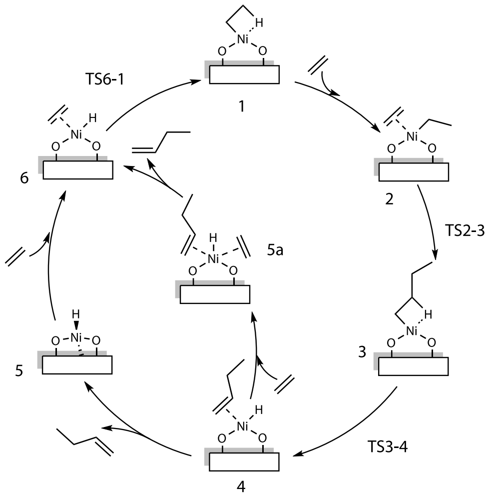

[a]The presentations of NU-1000's Zr_6O_8 node and organic linkers are omitted for simplicity.

similar methods and models to screen various transition metal-based SACs on the NU-1000 framework and demonstrated that Ni^{II}−NU-1000 was the most efficient catalyst for ethylene dimerization, whereas Cr^{II}, Co^{III}, and Pd^{II} analogues could be promising alternatives. Additionally, they pointed out that the inclusion of steric effects (by representing linkers adjacent to the active metal by benzoate groups) did not alter the free energy profiles. Similar formate cluster models were recently utilized to elucidate butene dimerization on UiO-66-supported catalysts.[23,24] A rare example where periodic models were used for ethylene dimerization was a work by Ye et al.,[17] in which they compared catalytic activity on a single Ni atom and Ni_4 cluster on NU-1000 and found that their activities toward ethylene dimerization were essentially similar.[16] The popularity of formate cluster models can be justified by an implicit assumption that the ethylene dimerization within MOF pores is negligibly hindered by organic linkers, given the smaller sizes of reactants and products when compared with a pore size. This assumption, however, remains to be validated. We note that for other reactions within MOFs, the utilization of extended models is more common,[25,26] although cluster models have also been shown to perform well.[27]

The second challenge in modeling reactions in MOF-based catalysts lies in the choice of the electronic structure method. So far, density functional theory methods have been employed as the main "workhorse" due to their great balance between cost and accuracy.[28,29] The aforementioned studies on NU-1000-supported SACs employed either GGA or *meta*-GGA functionals. Although DFT methods enable efficient explorations of chemical space and screenings for potential catalysts, they possess notorious limitations, particularly for systems prone to self-interaction errors (SIEs) and strong correlation effects,[30] such as MOFs. The accuracy of the DFT results depends on the choice of functionals, and thus a systematic comparison of the performance of different functionals is necessary. While DFT validations for catalytic reactions on zeolitic catalysts and other transition-metal-based systems are widely available,[31−36] such benchmarks remain scarce for MOF-based catalysts.[27,37−39] In recent work, when benchmarking the performance of 22 density functionals against experimental ethylene hydrogenation activation energies, Dohrmann et al. pointed out that in general, DFT methods failed to reproduce the experimental trend.[39]

Post-Hartree−Fock (post-HF) methods are expected to give more accurate results, since they are free from SIEs and can be systematically improved.[40] One of the most popular post-HF methods is CCSD(T). This method has high accuracy for systems where a single electronic configuration dominates, such as closed-shell molecules.[41,42] It provides excellent predictions for thermodynamic properties such as bond dissociation energies,[43] enthalpies,[44] and free energies.[45] Unfortunately, CCSD(T) can be computationally expensive when the molecular size increases, which limits its application to larger systems. The domain-based local pair natural orbital CCSD(T) or DLPNO−CCSD(T) is a cost-effective variation of CCSD(T) that introduces localization approximations for the most relevant electron pairs in a system to reduce computational demands without significantly sacrificing accuracy.[46] Several studies have demonstrated a good agreement between DLPNO−CCSD(T) with a tight threshold for the electron interactions and canonical CCSD(T) in predicting thermodynamic properties.[47] However, the use of tight settings for pair natural orbital (PNO) thresholds is important for obtaining accurate thermodynamic values.[48]

In this study, we revisit the ethylene dimerization reaction on a Ni(II) SAC supported on NU-1000 (hereafter termed Ni^{II}−NU-1000) via the Cossee-Arlman mechanism pathway. We aim to address the two aforementioned challenges, selecting the optimal computational model and determining the method for solving the electronic structure problem. Specifically, we compare the performance of different models at the GGA-DFT level to evaluate the effects of linkers on the stability of the stationary structures and the reaction's energetics. To improve the description of electronic structure energy, we devise a hybrid hierarchical cluster approach[35,49−56] to correct the relevant parts of the periodic model to the DLPNO−CCSD(T) level. We benchmark the performance of MP2 and 10 different DFT functionals with D3 correction, ranging from GGA (PBE[57]), *meta*-GGAs (TPSS,[58] M06-L[59]) to hybrids (TPSSh,[60] PBE0,[61] ωB97M,[62] M06,[63] BHandHLYP,[64] M06−2X,[65] and B3LYP[66]), within the correction scheme against the DLPNO−CCSD(T) energies. Although the benchmark has been done specifically for the ethylene dimerization reaction, we expect the findings from our study could generally be beneficial for similar catalytic reactions sharing similar critical steps, such as hydrogenation, C−C bond formation, or isomerization.

2. METHODOLOGY

2.1. Models. For the periodic calculations in this study, we adopted a unit cell of NU-1000 with the dimension of 39.90 Å × 39.90 Å × 16.50 Å, with $\alpha = \beta = 90°$ and $\gamma = 120°$, which are in good agreement with the experimental crystallographic parameters of 39.39 Å × 39.39 Å × 16.48 Å reported by Planas et al.[67] This unit cell includes three Zr_6O_8 clusters with staggered mixed proton arrangements,[67] on one of which a Ni atom is deposited. All atoms are allowed to relax during geometry optimizations.

Throughout this study, we employed several cluster models for different tasks. For exploring reaction mechanisms and assessing the performance of cluster models, shown in Section 3.1 and Section 3.2, we used the formate and benzoate models, where the organic linkers were represented by formate and benzoate groups, respectively.

As discussed in Section 3.2, for the benzoate model, we assessed two approaches: (i) assuming rigidity of the linkers by fixing the positions of the linker's carbon atoms or (ii) allowing partial flexibility of the linkers by constraining only *para*-carbon atoms in the phenyl rings to maintain the pseudolattice of the crystalline framework. In the formate model, the carbon atoms of the formate ligands were frozen during geometry optimization. All frozen atoms in both models were fixed to their respective positions in the optimized periodic NU-1000 structure described above. In the correction scheme in Section 3.3, several models, namely, formate and small models truncated from the respective periodic structure, were employed to calculate different components of the correction formula. More details on the construction of these small models and the corresponding calculations are given in Section S4.

2.2. Computational Details. *2.2.1. Optimization and Free Energy Calculations.* All the calculations in Section 3.1 and Section 3.2 were conducted using the Perdew−Burke−Ernzerhof (PBE) functional[57] with Grimme's D3 dispersion correction.[68,69] The calculations with the periodic model were conducted in the Vienna Ab Initio Simulation Package (VASP) code.[70−73] The Kohn−Sham equations were solved variationally in a plane-wave basis set by using the PAW method of Blöchl, as adapted by Kresse and Joubert with standard PAW potentials. A plane wave energy cutoff of 520 eV was used. The Brillouin zone was sampled at the Γ-point. Convergence criteria of 10^{-6} eV and 0.01 eV Å^{-1} were applied to SCF cycles and geometry optimizations, respectively, of all the intermediates and transition states (except for TS3−4, where a threshold of 0.02 eV Å^{-1} was used). The calculations with cluster models presented in Section 3.1 and Section 3.2 were done with the ORCA 5.0.3 program package[74] using PBE-D3(BJ), as used for the periodic model. The def2-TZVP basis set was applied for all atoms. Additionally, the effective core potentials were used for the Zr atoms.

For the periodic model, partial Hessian matrices were obtained numerically for part of the system resembling the formate model (without the additional hydrogen atoms), using the finite difference method in VASP with displacement steps of 0.01 Å. The resulting vibrational information was used for computing the thermochemical properties of the periodic model and the correction scheme, whereas analytical frequency calculations were performed for the finite cluster models to achieve their respective thermochemical properties. All eigenvalues for intermediates were confirmed to be positive, while each transition state was ensured to have exactly one negative eigenvalue. With exceptions with the rigid benzoate model, where an additional imaginary frequency corresponding to the hindered rotation of a constrained benzoate ligand was found for the structures. The harmonic oscillator approximation was employed to compute the thermochemical properties for intermediates and transitions. For gas-phase molecules, additional rigid-rotor and free-translator approximations were also applied.

2.2.2. Correction in the Hierarchical Cluster Approach. The correction scheme was implemented using the DFT, RI-MP2, and DLPNO−CCSD(T) methods,[46] as realized in the ORCA 5.0.4 program package.[74] Formate models of all intermediates and transition states were extracted from respective optimized periodic structures. Hydrogen atoms were added to saturate dangling bonds, and their positions were optimized at the PBE-D3(BJ)/def2-TZVP level.[75] Single-point energy calculations were performed on the optimized formate structures using the investigated methods.

In our hierarchical cluster approach, the corrected energy is calculated using a general form of eq 8, given as

$$E^{\mathrm{X}} = E_{\mathrm{pbc}}^{\mathrm{PBE-D3}} + \Delta E_{\mathrm{cluster}}^{\mathrm{X}} \tag{1}$$

where E^{X} is the energy corrected to the theory level X, $E_{\mathrm{pbc}}^{\mathrm{PBE\text{-}D3}}$ is the energy calculated using the periodic model at the PBE-D3 level, and $\Delta E_{\mathrm{cluster}}^{\mathrm{X}} = E_{\mathrm{cluster}}^{\mathrm{X}} - E_{\mathrm{cluster}}^{\mathrm{PBE\text{-}D3}}$ gives the correction from theory level *X* on the formate cluster. The $E_{\mathrm{cluster}}^{\mathrm{DLPNO-CCSD(T)}}$ term needed to obtain the reference energy is calculated via

$$\begin{aligned} E_{\mathrm{cluster}}^{\mathrm{DLPNO-CCSD(T)}} &= E_{\mathrm{cluster}}^{\mathrm{HF/CBS}} + E_{\mathrm{cluster}}^{\mathrm{CCSD(T)/hybrid}} \\ &\quad + \Delta E_{\mathrm{cluster}}^{\mathrm{MP2:DLPNO}} + \Delta E_{\mathrm{cluster}}^{\mathrm{MP2/CBS}} \end{aligned} \tag{2}$$

where $E_{\mathrm{cluster}}^{\mathrm{HF/CBS}}$ is energy at HF/CBS (extrapolation of def2 basis set family for cardinal numbers 3,4 using coefficients from Neese et al.[76] as it is encoded in ORCA), $E_{\mathrm{cluster}}^{\mathrm{CCSD}(T)\mathrm{/hybrid}}$ is the correlation energy of the coupled-cluster singles and doubles with the perturbative triples method, respectively, at the DLPNO−CCSD(T) level using the def2-QZVPP/def2-TZVP hybrid basis set (see details in Section S4), $\Delta E_{\mathrm{cluster}}^{\mathrm{MP2:DLPNO}}$ is the DLPNO truncation difference between MP2/def2-QZVPP and DLPNO-MP2/def2-QZVPP, and $\Delta E_{\mathrm{cluster}}^{\mathrm{MP2/CBS}}$ is the CBS extrapolation difference between MP2/def2-QZVPP and MP2/CBS.

For benchmarking DFs, various functionals were considered, including PBE, M06-L, TPSS, TPSSh, B3LYP, PBE0, ωB97M, M06, BHandHLYP, and M06-2X. Single-point calculations were carried out for each functional, all utilizing the def2-QZVPP basis set, with D3(BJ) (in the case of the M06 family, D3zero) dispersion corrections applied for improved accuracy for noncovalent interaction. We note in passing that the results obtained from M06-L, with and without dispersion correction, are virtually identical, showing slightly larger deviations for desorption barriers than for reaction barriers (Table S11).

3. RESULTS AND DISCUSSION

This section is structured as follows: First, we revise the Cossee-Arlman mechanism for the ethylene dimerization reaction on Ni$^{\mathrm{II}}$−NU-1000, highlighting the intricate coordination environment of the active metal sites and the role of agostic interactions. Then, we assess the performance of cluster models, namely, the formate and (rigid and pseudorigid) benzoate models, against the periodic counterpart at the PBE-D3(BJ) level. Afterward, we benchmark the performance of the MP2 method and several DFT functionals against the highly accurate DLPNO−CCSD(T) results.

3.1. Revised Cossee-Arlman Mechanism. The well-known Cossee-Arlman mechanism has long been posited as the dominant mechanism for ethylene dimerization catalyzed by nickel-based homo- and heterogeneous catalysts. The dimerization reaction on Ni$^{\mathrm{II}}$−NU-1000 was also widely reported to follow this linear chain growth pathway.[11,16] A schematic overview of this mechanism is shown in Scheme 1. In this subsection, we present a detailed analysis of the Cossee-Arlman dimerization mechanism on the Ni(II) SAC supported on NU-1000's zirconia nodes, considering two possible structures of Ni sites. The mechanistic results given in this

https://doi.org/10.1021/acs.jpcc.5c05954
J. Phys. Chem. C 2025, 129, 22377−22389

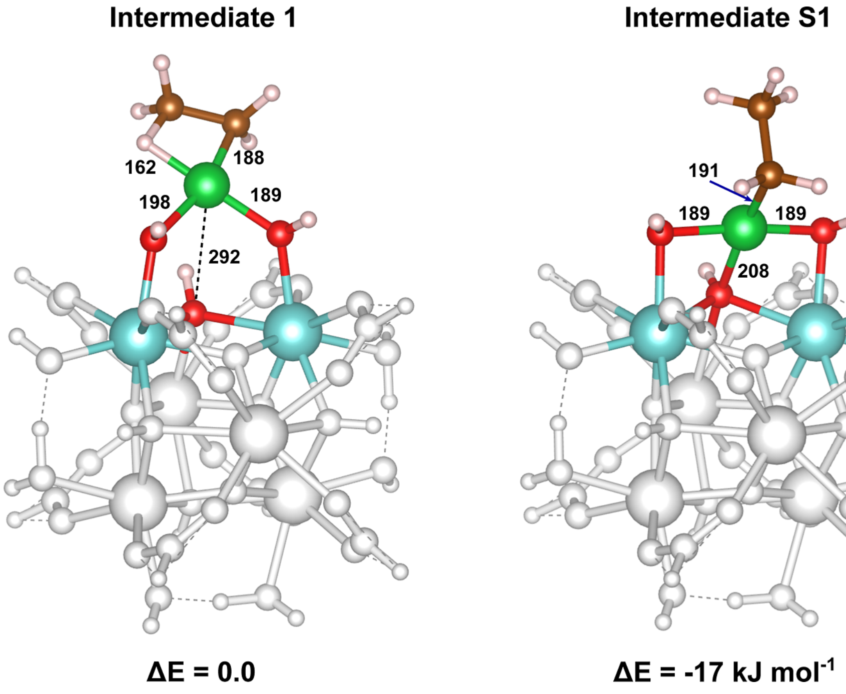

Figure 1. Two configurations of the [Ni-ethyl] structure: intermediate **1** (left) at the $Ni^{II}O_2$-type active site and intermediate **S1** (right) at the $Ni^{II}O_3$-type active site, together with their relative electronic energies. Representative chemical elements are represented by specific colors: Zr (cyan), Ni (green), O (red), C (brown), and H (light pink). The bond length and interatomic distances are given in pm.

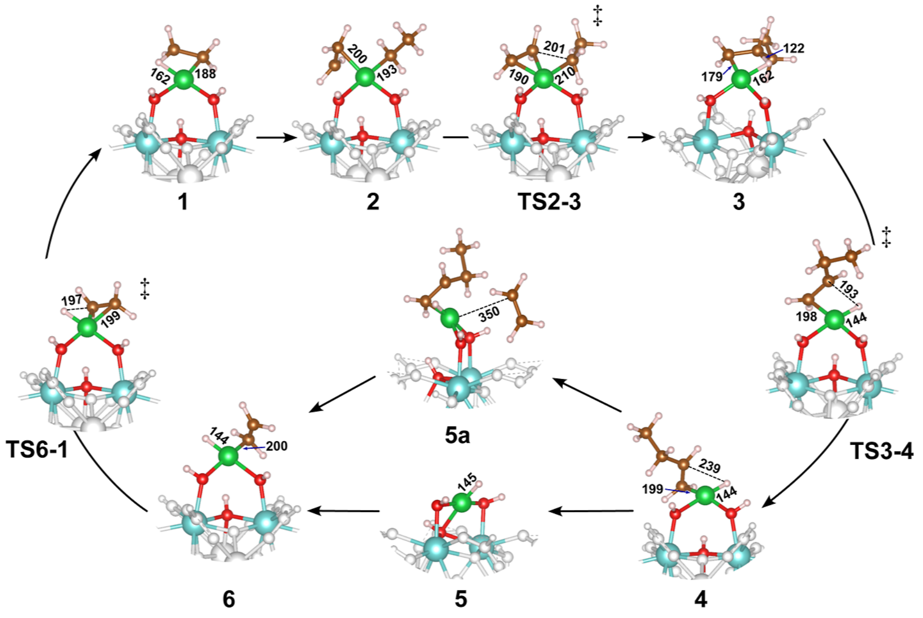

Figure 2. Key stationary structures involved in the ethylene dimerization reaction on the $Ni^{II}O_2$-type active site calculated at the PBE-D3(BJ)/def2-TZVP level using the formate cluster model. Representative chemical elements are represented by specific colors: Zr (cyan), Ni (green), O (red), C (brown), and H (light pink). The bond length and interatomic distances are given in pm.

subsection are explored using the formate cluster model (Figure 3c) at the PBE-D3(BJ)/def2-TZVP level.

We discovered that there could exist two types of active sites in the Ni^{II}−NU-1000 catalyst, in both of which the Ni center shows preferences for square planar configurations (Figure 1). The first type, hereafter termed the $Ni^{II}O_2$-type, corresponds to a more accessible active site where the Ni center is coordinated with two terminal hydroxo ligands, leaving space for two other coordinations. A representative structure of this type is intermediate **1**, which involves an agostic interaction between one β-hydrogen and the Ni atom, forming a bridging ethyl structure. Alternatively, the active site can reside closer to the Zr_6O_8 node (with shorter Ni−O bonds), coordinating with three μ−OH groups (thus referred to as $Ni^{II}O_3$-type) and one or two additional ligands (e.g., a terminal ethyl group in intermediate S1). Based on the Gibbs free energy profiles for the dimerization reaction on the two types of Ni active sites (Figure S1), it is found that the $Ni^{II}O_2$-type sites exhibit higher activity compared to their $Ni^{II}O_3$ counterpart. The enhanced activity is evident from the lower activation energies for the

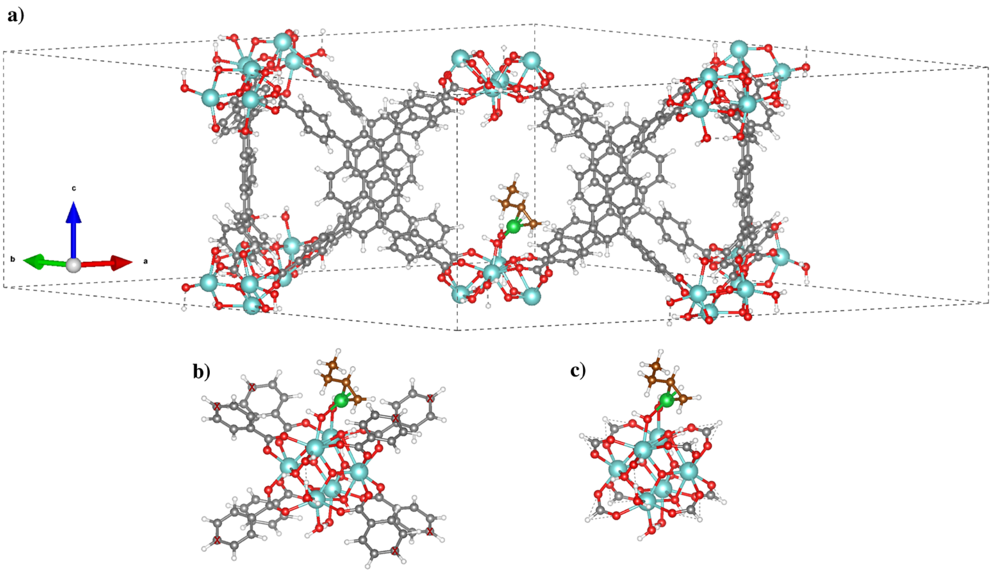

Figure 3. Three models used to simulate the catalytic performance of Ni^{II}−NU-1000. (a) Visualization of the MOF structure and the unit cell used for the periodic model consisting of three Zr_6O_8 nodes and one Ni active site, calculated in VASP; (b) benzoate model (the red crosses denote the *para*-carbon atoms being fixed in the pseudo-rigid variant); (c) formate model calculated using ORCA. In the visualization, different chemical elements are represented by specific colors: Zr (cyan), Ni (green), O (red), framework C (gray); reactive C (brown), and H (white).

ethylene insertion and β-hydride elimination reactions in the former site, which is primarily due to its increased accessibility and ability to maintain nickel's favorable square planar geometry throughout the catalytic cycle. Hence, we present a detailed analysis of the Cossee-Arlman mechanism on the $Ni^{II}O_2$-type active site (see Section S1 in Supporting Information for discussion on $Ni^{II}O_3$-type).

Figure 2 depicts the structures involved in the ethylene dimerization reaction on $Ni^{II}O_2$-type active sites in the Ni^{II}−NU-1000 catalyst. The corresponding free energy profile is given in Figure S1. The catalytic cycle begins with the [Ni-ethyl] species involving a bridging Ni−H agostic interaction (intermediate **1**). This contact is readily broken upon the approach of an ethylene molecule, forming a stable square planar π-complex **2** with an adsorption energy of −47 kJ mol^{1}. This structure is 38 kJ mol^{-1} more stable than the five-coordinated structure reported earlier.[11,17] The ethylene insertion takes place through a transition state **TS2−3** with coordination analogous to intermediate **2**. The activation free energy for C−C bond formation is about 84 kJ mol^{-1}. The tetracoordinated square Ni configuration is maintained in the [Ni-butyl] species **3** by the formation of a β-agostic hydrogen bridge, making this structure poised for the subsequent hydrogen elimination. The hydrogen abstraction requires an activation free energy of 33 kJ mol^{-1}, with the transition structure **TS3−4** resembling the square planar hydride product [H−Ni−But] **4**. Alternatively, the 1-butene product can be generated via a hydrogen transfer step in a [Et−Ni-butyl] species, producing [ethyl-Ni-But]. However, the barrier for this transfer is considerably higher than that of β-hydrogen elimination and will not be discussed further.

Following the hydrogen abstraction, newly formed 1-butene is released either via direct desorption or substitution with another ethylene molecule. An effective desorption barrier (i.e., **3** → **5**) of 62 kJ mol^{-1} is found for the direct route, while the latter route is energetically preferred by 23 kJ mol^{-1} at 298.15 K. This can be explained by the bare Ni-hydride species **5** undergoing structural transformation to a $Ni^{II}O_3$-type configuration in order to retain the square planar environment, which makes it unstable and leads to a considerable desorption energy. By contrast, the structure with an additional physisorbed ethylene **5a** is more stable because the [H−Ni−But] structure is preserved and the stabilizing dispersion effects are induced by the organic linkers. It is worth noting that such a desorption preference is entropy-dependent and relevant only at low temperatures and increased ethylene loadings (i.e., high ethylene pressures). The former route becomes dominant at temperatures above 380 K in ambient pressure (Figure S3). Finally, the active Ni-ethyl species is readily regenerated via ethylene hydrogenation (**5** → **1**) with a negligible activation energy of 6 kJ mol^{-1} and available to re-enter the cycle.

We note that for the reaction on this active site, the β-agostic interactions play a key role in maintaining the square planar environment in undercoordinated intermediates as well as in facilitating the product formation via hydrogen elimination. However, intermediates involving an agostic bond are less stable than those without them. In particular, the $Ni^{II}O_3$-type intermediate **S1** (Figure 1) is more stable ($\Delta E = -17$ kJ mol^{-1} and $\Delta G = -14$ kJ mol^{-1}) and, therefore, is more populated than the more active intermediate **1** (>300 times). The increased ethylene loadings (i.e., high ethylene pressure) could help to prevent the active intermediate **1** from restructuring into the **S1** structure by shifting the equilibrium **1** ⇌ **2** to the right, improving the catalyst's performance. Such an ethylene pressure dependence of the reaction rates was obtained experimentally for the Zr_6-based Ni/UiO-66 catalyst.[14] The increased mobility of Ni active sites regarding to excessive ethylene molecules was also observed for ethylene dimerization on Ni-SSZ-24 zeolite.[77]

Under the energetic span approximation proposed by Kozuch and Shaik,[78] the intermediate **2** and transition state **TS2−3** are the TOF-determining intermediate (TDI) and TOF-determining transition state (TDTS), respectively. Consequently, the C−C coupling step is the rate-determining state of the reaction. Note that the direct desorption state, whose effective activation free energy is 24 kJ mol^{-1} lower than that of the C−C coupling step, could potentially be an alternative rate-determining state, given the uncertainty in PBE energetics and inadequacy of the formate model. Therefore, despite being energetically less favorable at 298.15 K at the PBE-D3(BJ) level, this barrier will be considered in the following benchmarking of simulation models and density functionals, along with its substitutive counterpart and other TS-involved barriers.

3.2. Performance of Three Models. In Section 3.1, we employed a cluster model to thoroughly explore the nature of the active sites and the reaction mechanism. The use of truncated cluster models is widespread in the investigation of catalytic reactions in,[79,80] as it not only provides a computationally efficient approach to sampling the reaction network but also allows for high-level method treatments, often improving the electronic description. However, it should be noted that truncating a periodic model into a molecular cluster often leads to perturbed electronic properties and missing steric effects, especially when an improper truncation is made. Therefore, it is necessary to assess the performance of the common cluster models with respect to their extended periodic counterpart. For this, we employed a periodic model whose unit cell consists of three metal nodes, with the Ni active site residing on one of the nodes (Figure 3a) as the reference model. Using this model, we expect the steric effects to be fully captured. Two cluster models of the Zr_6O_8-based catalysts were evaluated, namely, the benzoate and formate models, in which the metal node and the active metal center were explicitly represented, while the organic linkers were truncated to benzoate or formate groups, respectively (Figure 3b,c). To preserve the rigidity of the framework, all carbon atoms of the benzoate and formate ligands were fixed to their positions, as in the optimized periodic NU-1000 structure. Here, the steric influences from the bulky linkers are assumed to be partially accounted for in the rigid benzoate model while completely ignored in the formate model. Alternatively, one can fix only positions of *para*-carbon atoms of the phenyl groups in the benzoate model, resulting in the so-called pseudo-rigid benzoate model. This model allows the aromatic rings to rotate, mimicking the linkers' flexibility in the extended model, while retaining the pseudo-lattice of the MOF structure.[80]

For evaluating models' performances, we compare the activation energy of the following five steps/states that are mechanistically relevant for the ethylene dimerization catalyzed on Ni^{II}−NU-1000:

1. C−C coupling

[Et-Ni-ethyl] → [Ni-butyl],

$$\Delta\Delta E_1^{\ddagger} = \Delta E(\mathbf{TS2\text{-}3}) - \Delta E(\mathbf{2}) \tag{3}$$

2. *β*-H elimination

[Ni-butyl] → [H-Ni-But],

$$\Delta\Delta E_2^{\ddagger} = \Delta E(\mathbf{TS3\text{-}4}) - \Delta E(\mathbf{3}) \tag{4}$$

3. Direct but-1-ene desorption

[Ni-butyl] → [Ni-H] + $\dot{C}_4\dot{H}_{8(\mathbf{g})}$,

$$\Delta\Delta E_3^{\ddagger} = \Delta E(\mathbf{5}) + \Delta E(\dot{C}_4\dot{H}_8) - \Delta E(\mathbf{3}) \tag{5}$$

4. Substitutive but-1-ene desorption

[Ni-butyl] → [H-Ni-But] + $\dot{C}_4\dot{H}_{8(\mathbf{ph})}$,

$$\Delta\Delta E_5^{\ddagger} = \Delta E(\mathbf{5a}) - \Delta E(\mathbf{3}) \tag{6}$$

5. Ethylene hydrogenation

[H-Ni-Et] → [Ni-ethyl],

$$\Delta\Delta E_5^{\ddagger} = \Delta E(\mathbf{TS6\text{-}1}) - \Delta E(\mathbf{6}) \tag{7}$$

where (**g**) and (**ph**) subscripts denote the gas-phase and the physisorbed molecules, respectively. Table 1 presents these energy barriers predicted at the PBE-D3(BJ) level (see Figure S4 and Table S1 for the relative energy profile and full energetic data). The Gibbs free energy barriers can be obtained using equations analogous to eqs 3−7, with *G* replacing *E*. It is worth noting that the free energies of desorption are largely dependent on the entropic effects, whereas those of elementary reactions (i.e., involving TS) are less sensitive to entropy. As a result, the desorption activation energies reported in Table 1 differ substantially from their corresponding free energies (Table S2). However, comparing these models based on their free energy data at a given temperature is not straightforward. To ensure a consistent comparison across models, we focus on the activation energies rather than the activation free energies. Nevertheless, for completeness, we also present the free energy profiles at 298.15 K in Figure S5.

Table 1. Electronic Energy Barriers in kJ mol^{-1} at PBE-D3/def2-TZVP or PBE-D3/PP for the Most Important Mechanistic States Calculated from eqs 3−7 Using Different Simulation Models

reaction	pbc	pseudo-rigid benzoate	rigid benzoate	formate
C−C coupling	82	79	78	83
β-H elimination	40	44	45	30
ethylene hydrogenation	8	12	9	4
direct desorption	129	123	128	121
substitutive desorption	−5	−2	−3	−1

In general, all examined cluster models yield results that are comparable to those of the extended model with mean absolute deviations typically smaller than 4 kJ mol^{-1}. Consequently, the overall reaction mechanism is well reproduced by these truncated models. This consistency probably reflects the localized nature of the electronic structure in the Ni^{II}−NU-1000 system, suggesting that truncation of the periodic structure does not significantly perturb its electronic properties. However, in some cases, deviations are non-negligible. In addition to truncation-induced electronic errors, another source can be varying degrees of steric interactions associated with each model. To evaluate the impact of the two factors, we further examine the deviations across the three cluster models. The most notable differences in the activation energies are observed for *β*-hydride abstraction and direct desorption predicted by the formate model. This smallest model underestimates the two barriers by 10 and 8 kJ mol^{-1}, respectively. This underestimation arises primarily from the model's failure to account for the dispersion interactions between the Ni-butyl fragment and the ligand environment in intermediate **3**, which associates with both barriers (Table S1). As a result, the stability of intermediate **3** is overestimated by 7 kJ mol^{-1}, which translates to an underestimation of associated barriers by the same amount. A closer examination of the stability of adsorbed intermediates (Table S1) further underscores this limitation of the formate model, as its predicted energies are generally higher than those of the periodic model, particularly for sterically demanding structures. Therefore, the errors in activation energies of cluster models are more likely attributable to the inadequate description of the steric environment.

Increasing the steric effects in the cluster model (i.e., by including linker's benzene rings) improves the energy predictions. In particular, the rigid benzoate model yields reaction barriers that deviate within 5 kJ mol^{-1} from those obtained using periodic boundary conditions, with a MAD as low as 2.5 kJ mol^{-1}. Further improving the ligands' flexibility using the pseudo-rigid model does not enhance the electronic description, as highlighted by the prediction for the direct 1-butene desorption, with a deviation of 6 kJ mol^{-1}. Nonetheless, both benzoate models outperform the formate model. This improved performance can be ascribed to their enhanced ability to capture dispersion interactions, as demonstrated in the dispersion corrections that are closer to those of the periodic model (Table S3). While both benzoate models give comparable accuracy in electronic energy prediction, the pseudo-rigid variant offers a practical advantage, as it is often free from residual imaginary frequencies corresponding to vibrational modes coupled to the constrained ligands. This issue, common when rigid models are used, often leads to inaccurate thermochemical results obtained via harmonic oscillator approximation. Therefore, the pseudo-rigid benzoate model can be considered to be a more suitable and reliable representation of the Ni^{II}−NU-1000 catalyst for this reaction.

3.3. Performance of Density Functionals. While the periodic model is capable of capturing the full steric effects on the reactive regions, it is largely limited to the use of GGA functionals. On the other hand, as shown in Section 3.2, the electronic structure of the Ni^{II}−NU-1000 system is highly localized, implying that predictions' accuracy can be enhanced by treating the most catalytically important region of the system with a more accurate method. To this end, we corrected the energy predictions to the coupled cluster level by employing the DLPNO−CCSD(T) method on the formate cluster truncated from the corresponding periodic structure (c.f., Sections 2 and S4). This constitutes a hierarchical cluster approach, which has been commonly adopted for zeolitic systems.[34,35,49−53] Our hierarchical approach can be considered an "ideal model" for obtaining highly accurate results in MOF-based catalysis.[80] With the coupled cluster results as a reference, we aim to evaluate the performance of various density functionals (DFs) within this approach for the ethylene dimerization reaction. It is important to note the system under investigation exhibits single-reference character (c.f., Section S3), and therefore, the DLPNO−CCSD(T) method should serve as a reliable reference.

The reference values for the energies of intermediates and transition states are given by

$$E = E_{\text{pbc}}^{\text{PBE-D3}} + \Delta E_{\text{cluster}}^{\text{CC}} \tag{8}$$

where $E_{\text{pbc}}^{\text{PBE=D3}}$ is the energy calculated using the periodic model at PBE-D3 level, and $\Delta E_{\text{cluster}}^{\text{CC}} = E_{\text{cluster}}^{\text{DLPNO−CCSD(T)}} - E_{\text{cluster}}^{\text{PBE-D3}}$ gives the correction from DLPNO−CCSD(T) on the mentioned formate cluster (a detailed description of $E_{\text{cluster}}^{\text{DLPNO-CCSD(T)}}$ is given the Section 2). The results from different DFs under the hierarchical cluster approach were obtained via an equation similar to that in eq 8, with the ΔE term calculated for each respective functional. All absolute electronic energy and relative energy values, taking intermediate **1** as the reference (zero), obtained from the coupled cluster reference method and various DFs, is tabulated in Tables S8 and S9, respectively.

Figure 4a−c shows the accuracy of several DFs and the MP2 method in terms of mean absolute deviation (MAD) and mean signed deviation (MSD), evaluated for the energies of adsorbed intermediates, transition states, and all of the stationary points along the reaction pathway, respectively. The PBE functional systematically overestimates the stability of both intermediates and transition states, yielding an overall MAD of 14 kJ mol^{-1}, with a larger MAD observed for transition states (20 kJ mol^{-1}). Most *meta*-GGA and hybrid functionals provide reasonably accurate energy predictions, with overall deviations generally below 11 kJ mol^{-1}. Among them, the best performing functionals are TPSSh, PBE0, and M06-L, whose overall MADs fall in the range of 5−6 kJ mol^{-1}. Notably, increasing the fraction of exact exchange deteriorates accuracy, as evidenced by the remarkably larger MADs of approximately 30 kJ mol^{-1} for BHandHLYP and M06-2X, which contain 50 and 54% HF-exchange, respectively. The MP2 method fails to provide reliable results for this dimerization reaction, highlighting the important role of higher-order electron correlation effects. The MSD data further reveal systematic trends. The GGA and *meta*-GGA functionals tend to underestimate the energies, while hybrid functionals are more likely to overestimate them. Such propensities are observed for both intermediates and transition states.

It is worth noting that transition state energies are generally more difficult to predict than adsorbed intermediates, as demonstrated in larger MADs in all of the examined methods. This observation is consistent with previous benchmarks on other catalytic systems.[34] However, the accuracy of activation energy predictions often benefits from the fact that transition states and corresponding intermediates have the same signed deviations (both overstabilized and both understabilized), resulting in the so-called error cancellations. Consequently, the predicted energy barriers evaluated by a given functional may be more accurate than the predictions for the relevant transition states and intermediates. In order to elucidate this point, we plot in Figure 5 the activation free energy values of the important states discussed in Section 3.2 from some selected DFs and the deviation statistics of all benchmarked methods. Note that the same partial Hessians obtained at the periodic PBE-D3 level were used to estimate the Gibbs free energies for all DFs presented in Figure 5a, and therefore, the deviations essentially stem from electronic energy differences (see Figure S9).

As seen in Figure 5a, the GGA, *meta*-GGA, and hybrid functionals with low proportions of HF exchange generally yield more accurate C−C coupling barriers compared to those with higher exchange contributions. The β-hydrogen elimination reaction is particularly challenging to model, as only three functionals, namely, M06-L, TPSSh, and B3LYP, are able to reproduce the reference barrier within 5 kJ mol^{-1}. The GGA and *meta*-GGA functionals tend to underestimate the barrier, while hybrid functionals generally overestimate it. All selected DFs perform reasonably well for the ethylene hydrogenation

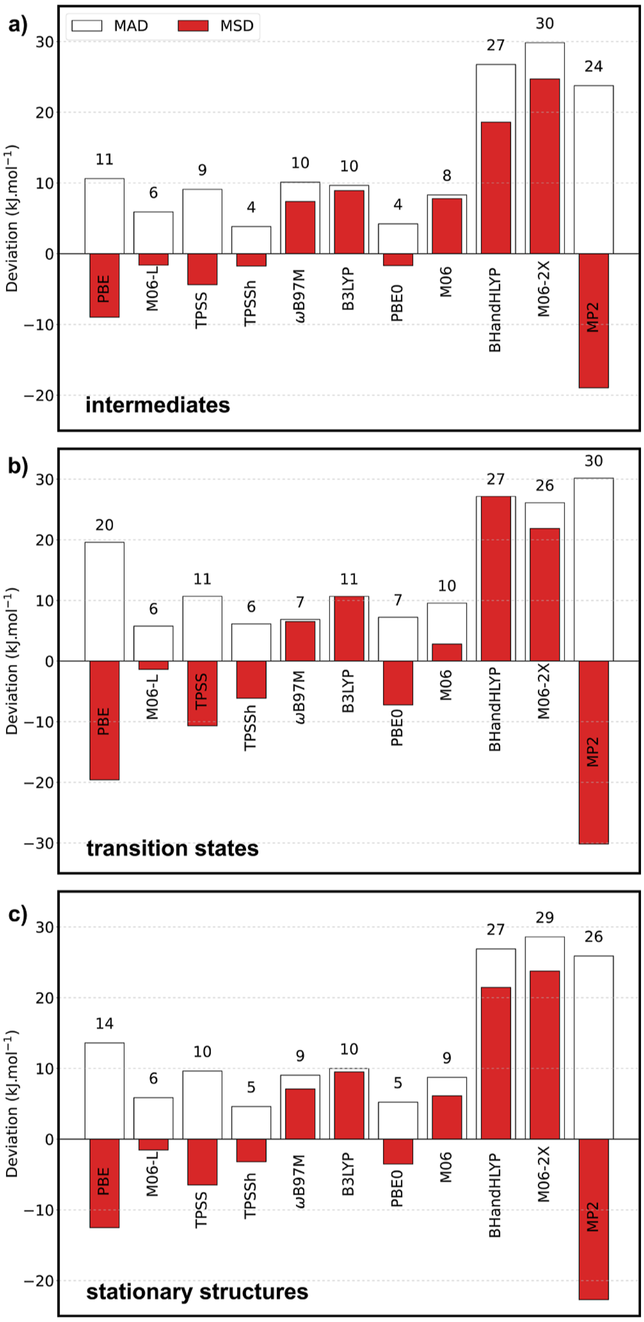

Figure 4. Accuracy of the MP2 method and different density functionals for ethylene dimerization on Ni^{II}−NU-1000 catalyst, evaluated in terms of mean absolute deviation (MAD) and mean signed deviation (MSD) with respect to the coupled cluster reference. (a,b) Deviations in energies of intermediates and transition states, respectively, relative to intermediate **1**; (c) Overall deviations, taking into account all intermediates and transition states. The number above each bar denotes the corresponding MAD (in kJ mol^{-1}). All DFT calculations were performed with the D3 dispersion correction.

reaction, aligned with the observation by Benali et al.[81] The two desorption barriers are also challenging, with TPSSh providing the most reliable predictions.

Figure 5b shows that TPSSh performs best in predicting energy barriers, followed by M06-L. B3LYP benefits significantly from error cancellation in the TS-involved barriers, achieving a remarkably low MAD* of 2 kJ mol^{-1} despite its overall energy MAD of 10 kJ mol^{-1} (Figure 4c).

Due to error cancellation, most of the DFs in Figure 5 are able to offer a qualitatively correct mechanistic picture of the ethylene dimerization reaction on Ni^{II}−NU-1000. However, when deviations of transition states and intermediates are of different signs, one ends up with increased rather than reduced deviations. For example, although the statistics for PBE0 in Figure 4 might suggest reasonable accuracy, the reaction mechanism predicted by this functional deviates from the reference. All PBE0 barriers, except for hydrogenation, deviate within the 10 kJ mol^{-1} range, making mechanistic interpretation inconclusive, considering the inherent uncertainty of DFT.

The calculated reaction energies and barriers are often used to predict reaction rates via kinetic models to compare theoretical predictions to experimental results. To achieve the best agreement with experiments, high accuracy in both relative energy and barrier predictions is highly desirable. Among the tested functionals, TPSSh and M06-L demonstrate the best performance, with TPSSh slightly outperforming. This finding supports the widespread use of the M06-L functional for modeling catalysis in NU-1000 and other Zr-based MOFs.[10,11,16,17,82−85]

Finally, we plot in Figure 6 the Gibbs free energy profile at 298.15 K for ethylene dimerization on Ni^{II}−NU-1000 obtained using the best DFT functional, identified in our benchmarking, namely TPSSh. The ethylene insertion barrier remains the rate-determining state with an activation energy of 77 kJ mol^{-1}. The β-hydrogen abstraction activation energy is moderate (41 kJ mol^{-1}) while the hydrogenation barrier is readily overcome. The desorption of the 1-butene is expected to occur via substitution of an incoming ethylene molecule, while a direct desorption is nearly 15 kJ mol^{-1} less preferred.

Our most accurate DFT activation free energy for the rate-determining state is approximately 20 kJ mol^{-1} higher than the M06-L values reported in literature using cluster models.[11,17] The discrepancy in computational values, however, arises mainly from a new stable structure identified for intermediate **2**, rather than from differences in the accuracy of the computational method. The Ni SAC supported on NU-1000, while still active for ethylene dimerization, exhibits lower activity than previously predicted. To further compare with previous theoretical and experimental data, we compute turnover frequencies (TOFs) at 298.15 K and 1 atm using the energetic span approximation[78] via

$$\mathrm{TOF} = \frac{k_B T}{h}\exp\left(\frac{-\delta G}{RT}\right) \tag{9}$$

where δG is the energetic span, which, for our reaction, is the activation free energy of the rate-determining state, k_B is the Boltzmann constant, h is the Planck constant, R is the gas constant, and T is the temperature. The results predicted by all examined methods are listed in Table S10. The coupled cluster approach predicts a TOF of 260 h^{-1}, in great agreement with the experimental value of 252 h^{-1},[10] while our best functional, TPSSh, also provides a reasonable prediction of 612 h^{-1}. These values are 3 orders of magnitude smaller than those previously predicted in the literature.[16]

4. CONCLUSIONS

In this study, we have thoroughly investigated the ethylene dimerization via the linear insertion pathway (Cossee-Arlman mechanism) on a Ni single-atom catalyst supported in NU-

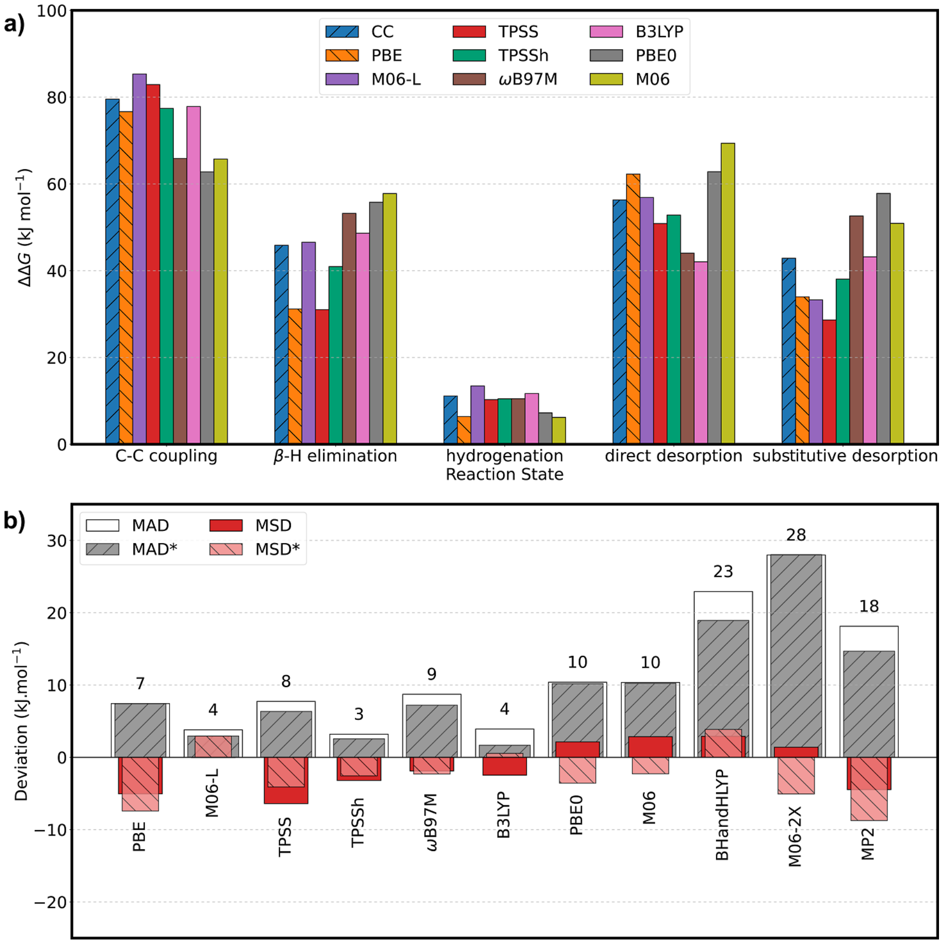

Figure 5. (a) Comparison of activation free energies in kJ mol^{-1} of important mechanistic states estimated by several selected DFs within the hierarchical cluster approach. (b) Accuracy of MP2 and DFs in terms of mean absolute deviation (MAD) and mean signed deviation (MSD) with respect to the coupled cluster reference. The MAD* and MSD* consider only the TS-involved barriers, whereas MAD and MSD represent the deviations for the five barriers discussed in Section 3.2. The number above each bar denotes the corresponding MAD (in kJ mol^{-1}). All DFT calculations were performed with the D3 dispersion correction.

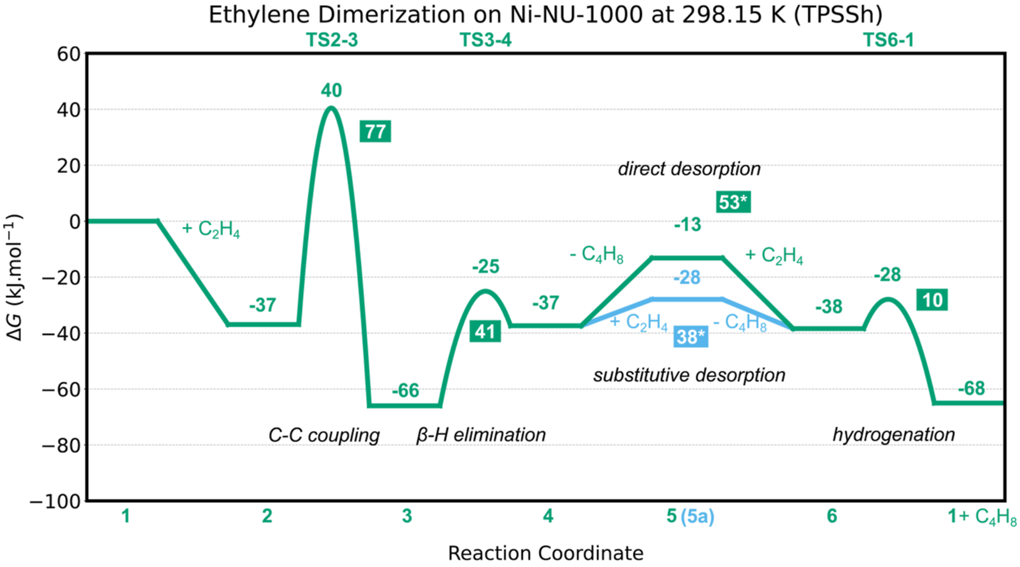

Figure 6. Gibbs free energy profile at 298.15 K for the ethylene dimerization reaction on Ni^{II}−NU-1000 obtained at the TPSSh-D3(BJ) level within the hierarchical cluster approach. This profile is the most accurate result predicted by examined DFs with respect to the coupled cluster reference. The framed values are the activation free energy for each reaction state, in which the asterisk denotes an effective desorption barrier, defined in Section 3.2.

1000 by DFT methods. We provide atomistic insights into the nature of the mononuclear Ni sites and their catalytic transformations along the reaction pathway. The adequacy of truncated cluster models and the accuracy of different density functionals in describing the reaction were benchmarked against highly accurate and computationally demanding models and methods, respectively.

Using a formate cluster model at the PBE-D3(BJ) level, we have identified two stable motifs of the mononuclear Ni active sites that could exist simultaneously on NU-1000s zirconia nodes and catalyze the dimerization reaction via the Cossee-Arlman mechanism. While the $Ni^{II}O_3$ sites are energetically more stable, the $Ni^{II}O_2$ counterparts are catalytically more active and, thus, act as the primary active sites. High ethylene pressure and an β-agostic bond are found to play a key role in preserving the square planar environment of the under-coordinated $Ni^{II}O_2$ catalyst across the catalytic cycle. Furthermore, the agostic bond also facilitates the β-hydrogen abstraction reaction in the $Ni^{II}O_2$ sites. The ethylene pressure also influences the desorption of the butene product at the temperature of interest, as high pressure facilitates the energetically favorable substitutive desorption.

The examined truncated models are all capable of providing results that are in qualitative agreement with that of the extended periodic model, which highlights the highly localized electronic structure of the catalytic system and minimal role of steric effects. The recovery of steric interactions, particularly in spatially demanding structures, is enhanced by introducing better linker representations, resulting in benzoate models outperforming their formate counterparts in predicting key activation energies. The pseudo-rigid model, however, is practically more advantageous, as it often gives a clean vibrational spectrum, beneficial to computing thermochemical properties, such as Gibbs free energy.

The reaction energetics were found to be more sensitive to the choice of electronic structure method than to the simulation model. Transition state energies are generally more difficult to predict exactly using DFT than those of adsorbed intermediates, and the DFT energy barriers often benefit from error cancellation. Overall, the best performance in describing both reaction energies and barriers was achieved by using TPSSh and M06-L functionals. These results provide theoretical support for the common use of cluster models and the M06-L method in computational studies of catalysis in Zr-based MOFs. Additionally, our finding reveals that all tested GGA, *meta*-GGA, and hybrid functionals with exact exchange fractions below 50% (except for PBE0) can be employed for the qualitative exploration of the reaction mechanisms. In particular, the PBE functional, despite showing large deviations in relative energies, systematically underestimates barriers of TS-related reactions, with a MAD of less than 8 kJ mol^{-1}.

Finally, owing to the comprehensive consideration of the factors discussed above, our best predictions successfully reproduced the experimental TOF. Given the scarcity of similar benchmarks for MOF systems, we expect our approach and benchmarking results to be valuable for studying catalytic processes in this class of materials.

■ ASSOCIATED CONTENT

Supporting Information

The Supporting Information is available free of charge at https://pubs.acs.org/doi/10.1021/acs.jpcc.5c05954.

Further information on the Cossee-Arlman mechanism on $Ni^{II}O_3$-type active sites, energies and free energies for benchmarked models and DFs, multireference analysis, technical details of the hierarchical cluster approach, and TOF estimations (PDF)

All data used to support the conclusions of this work, including all coordinates, energies, and vibrational frequencies (ZIP)

■ AUTHOR INFORMATION

Corresponding Authors

Karin Fink − *Institute of Nanotechnology, Karlsruhe Institute of Technology, 76344 Karlsruhe, Germany*; Email: karin.fink@kit.edu

Dmitry I. Sharapa − *Institute of Catalysis Research and Technology, Karlsruhe Institute of Technology, 76344 Karlsruhe, Germany*; orcid.org/0000-0001-9510-9081; Email: dmitry.sharapa@kit.edu

Authors

Thanh-Nam Huynh − *Institute of Catalysis Research and Technology, Karlsruhe Institute of Technology, 76344 Karlsruhe, Germany*

Nikita A. Matsokin − *Institute of Nanotechnology, Karlsruhe Institute of Technology, 76344 Karlsruhe, Germany*

Felix Studt − *Institute of Catalysis Research and Technology, Karlsruhe Institute of Technology, 76344 Karlsruhe, Germany; Institute for Chemical Technology and Polymer Chemistry, Karlsruhe Institute of Technology, 76131 Karlsruhe, Germany*; orcid.org/0000-0001-6841-4232

Complete contact information is available at: https://pubs.acs.org/10.1021/acs.jpcc.5c05954

Author Contributions

[‖]T.-N.H. and N.A.M. contributed equally to this work.

Notes

The authors declare no competing financial interest.

■ ACKNOWLEDGMENTS

The authors gratefully acknowledge support from the GRK 2450 and the state of Baden-Württemberg via access to the bwHPC (bwUnicluster) and the German Research Foundation (DFG) through grant no. INST 40/575-1 FUGG (JUSTUS 2 cluster, RVs bw17D011 and bw15C003). Additionally, the work was partially performed on the HoReKa supercomputer funded by the Ministry of Science, Research, and the Arts Baden-Württemberg and by the Federal Ministry of Education and Research.

■ REFERENCES

(1) Lee, J.; Farha, O. K.; Roberts, J.; Scheidt, K. A.; Nguyen, S. T.; Hupp, J. T. Metal−organic framework materials as catalysts. *Chem. Soc. Rev.* **2009**, *38*, 1450.

(2) Bavykina, A.; Kolobov, N.; Khan, I. S.; Bau, J. A.; Ramirez, A.; Gascon, J. Metal−Organic Frameworks in Heterogeneous Catalysis: Recent Progress, New Trends, and Future Perspectives. *Chem. Rev.* **2020**, *120*, 8468−8535.

(3) Alzamly, A.; Bakiro, M.; Hussein Ahmed, S.; Siddig, L. A.; Nguyen, H. L. Linear α-olefin oligomerization and polymerization catalyzed by metal-organic frameworks. *Coord. Chem. Rev.* **2022**, *462*, 214522.

(4) Nicholas, C. P. Applications of light olefin oligomerization to the production of fuels and chemicals. *Appl. Catal., A* **2017**, *543*, 82−97.

(5) Gogate, M. R. Methanol-to-olefins process technology: current status and future prospects. *Pet. Sci. Technol.* **2019**, *37*, 559−565.

(6) Yang, M.; Fan, D.; Wei, Y.; Tian, P.; Liu, Z. Recent Progress in Methanol-to-Olefins (MTO) Catalysts. *Adv. Mater.* **2019**, *31*, 1902181.

(7) Canivet, J.; Aguado, S.; Schuurman, Y.; Farrusseng, D. MOF-Supported Selective Ethylene Dimerization Single-Site Catalysts through One-Pot Postsynthetic Modification. *J. Am. Chem. Soc.* **2013**, *135*, 4195−4198.

(8) Madrahimov, S. T.; Gallagher, J. R.; Zhang, G.; Meinhart, Z.; Garibay, S. J.; Delferro, M.; Miller, J. T.; Farha, O. K.; Hupp, J. T.; Nguyen, S. T. Gas-Phase Dimerization of Ethylene under Mild Conditions Catalyzed by MOF Materials Containing (bpy)Ni^{II} Complexes. *ACS Catal.* **2015**, *5*, 6713−6718.

(9) Metzger, E. D.; Brozek, C. K.; Comito, R. J.; Dincă, M. Selective Dimerization of Ethylene to 1-Butene with a Porous Catalyst. *ACS Cent. Sci.* **2016**, *2*, 148−153.

(10) Li, Z.; Schweitzer, N. M.; League, A. B.; Bernales, V.; Peters, A. W.; Getsoian, A. B.; Wang, T. C.; Miller, J. T.; Vjunov, A.; Fulton, J. L.; Lercher, J. A.; Cramer, C. J.; Gagliardi, L.; Hupp, J. T.; Farha, O. K. Sintering-Resistant Single-Site Nickel Catalyst Supported by Metal−Organic Framework. *J. Am. Chem. Soc.* **2016**, *138*, 1977−1982.

(11) Bernales, V.; League, A. B.; Li, Z.; Schweitzer, N. M.; Peters, A. W.; Carlson, R. K.; Hupp, J. T.; Cramer, C. J.; Farha, O. K.; Gagliardi, L. Computationally Guided Discovery of a Catalytic Cobalt-Decorated Metal−Organic Framework for Ethylene Dimerization. *J. Phys. Chem. C* **2016**, *120*, 23576−23583.

(12) Mondloch, J. E.; Bury, W.; Fairen-Jimenez, D.; Kwon, S.; DeMarco, E. J.; Weston, M. H.; Sarjeant, A. A.; Nguyen, S. T.; Stair, P. C.; Snurr, R. Q.; Farha, O. K.; Hupp, J. T. Vapor-Phase Metalation by Atomic Layer Deposition in a Metal−Organic Framework. *J. Am. Chem. Soc.* **2013**, *135*, 10294−10297.

(13) Cavka, J. H.; Jakobsen, S.; Olsbye, U.; Guillou, N.; Lamberti, C.; Bordiga, S.; Lillerud, K. P. A New Zirconium Inorganic Building Brick Forming Metal Organic Frameworks with Exceptional Stability. *J. Am. Chem. Soc.* **2008**, *130*, 13850−13851.

(14) Yeh, B.; Vicchio, S. P.; Chheda, S.; Zheng, J.; Schmid, J.; Löbbert, L.; Bermejo-Deval, R.; Gutiérrez, O. Y.; Lercher, J. A.; Lu, C. C.; Neurock, M.; Getman, R. B.; Gagliardi, L.; Bhan, A. Site Densities, Rates, and Mechanism of Stable Ni/UiO-66 Ethylene Oligomerization Catalysts. *J. Am. Chem. Soc.* **2021**, *143*, 20274−20280.

(15) Yeh, B.; Chheda, S.; Zheng, J.; Schmid, J.; Löbbert, L.; Bermejo-Deval, R.; Gutiérrez, O. Y.; Lercher, J. A.; Gagliardi, L.; Bhan, A. Validation of the Cossee−Arlman mechanism for propylene oligomerization on Ni/UiO-66. *Catal. Sci. Technol.* **2023**, *13*, 4213−4222.

(16) Ye, J.; Gagliardi, L.; Cramer, C. J.; Truhlar, D. G. Single Ni atoms and Ni_4 clusters have similar catalytic activity for ethylene dimerization. *J. Catal.* **2017**, *354*, 278−286.

(17) Ye, J.; Gagliardi, L.; Cramer, C. J.; Truhlar, D. G. Computational screening of MOF-supported transition metal catalysts for activity and selectivity in ethylene dimerization. *J. Catal.* **2018**, *360*, 160−167.

(18) Goetjen, T. A.; Zhang, X.; Liu, J.; Hupp, J. T.; Farha, O. K. Metal−Organic Framework Supported Single Site Chromium(III) Catalyst for Ethylene Oligomerization at Low Pressure and Temperature. *ACS Sustainable Chem. Eng.* **2019**, *7*, 2553−2557.

(19) Kømurcu, M.; Lazzarini, A.; Kaur, G.; Borfecchia, E.; Øien Ødegaard, S.; Gianolio, D.; Bordiga, S.; Lillerud, K. P.; Olsbye, U. Co-catalyst free ethene dimerization over Zr-based metal-organic framework (UiO-67) functionalized with Ni and bipyridine. *Catal. Today* **2021**, *369*, 193−202.

(20) Goetjen, T. A.; Ferrandon, M. S.; Kropf, A. J.; Lamb, J. V.; Delferro, M.; Hupp, J. T.; Farha, O. K. Active-Site Determination and Mechanistic Insights in a MOF-Supported Polymerization Catalyst. *J. Phys. Chem. C* **2022**, *126*, 20388−20394.

(21) Goetjen, T. A.; Knapp, J. G.; Syed, Z. H.; Hackler, R. A.; Zhang, X.; Delferro, M.; Hupp, J. T.; Farha, O. K. Ethylene polymerization with a crystallographically well-defined metal−organic framework supported catalyst. *Catal. Sci. Technol.* **2022**, *12*, 1619−1627.

(22) Rajapaksha, R.; Samanta, P.; Quadrelli, E. A.; Canivet, J. Heterogenization of molecular catalysts within porous solids: the case of Ni-catalyzed ethylene oligomerization from zeolites to metal−organic frameworks. *Chem. Soc. Rev.* **2023**, *52*, 8059−8076.

(23) Zheng, J.; et al. Metal-organic framework supported single-site nickel catalysts for butene dimerization. *J. Catal.* **2022**, *413*, 176−183.

(24) Löbbert, L.; Chheda, S.; Zheng, J.; Khetrapal, N.; Schmid, J.; Zhao, R.; Gaggioli, C. A.; Camaioni, D. M.; Bermejo-Deval, R.; Gutiérrez, O. Y.; Liu, Y.; Siepmann, J. I.; Neurock, M.; Gagliardi, L.; Lercher, J. A. Influence of 1-Butene Adsorption on the Dimerization Activity of Single Metal Cations on UiO-66 Nodes. *J. Am. Chem. Soc.* **2023**, *145*, 1407−1422.

(25) Vermoortele, F.; Bueken, B.; Le Bars, G.; Van de Voorde, B.; Vandichel, M.; Houthoofd, K.; Vimont, A.; Daturi, M.; Waroquier, M.; Van Speybroeck, V.; Kirschhock, C.; De Vos, D. E. Synthesis Modulation as a Tool To Increase the Catalytic Activity of Metal−Organic Frameworks: The Unique Case of UiO-66(Zr). *J. Am. Chem. Soc.* **2013**, *135*, 11465−11468.

(26) Ortuño, M. A.; Rellán-Piñeiro, M.; Luque, R. Computational Mechanism of Methyl Levulinate Conversion to γ-Valerolactone on UiO-66 Metal Organic Frameworks. *ACS Sustainable Chem. Eng.* **2022**, *10*, 3567−3573.

(27) Le, T.-H. T.; Ferro-Costas, D.; Fernández-Ramos, A.; Ortuño, M. A. Combined DFT and Kinetic Monte Carlo Study of UiO-66 Catalysts for γ-Valerolactone Production. *J. Phys. Chem. C* **2024**, *128*, 1049−1057.

(28) Bursch, M.; Mewes, J.; Hansen, A.; Grimme, S. Best-Practice DFT Protocols for Basic Molecular Computational Chemistry. *Angew. Chem.* **2022**, *134*, No. e202205735.

(29) Teale, A. M.; et al. DFT exchange: sharing perspectives on the workhorse of quantum chemistry and materials science. *Phys. Chem. Chem. Phys.* **2022**, *24*, 28700−28781.

(30) Mardirossian, N.; Head-Gordon, M. Thirty years of density functional theory in computational chemistry: an overview and extensive assessment of 200 density functionals. *Mol. Phys.* **2017**, *115*, 2315−2372.

(31) Hemelsoet, K.; Lesthaeghe, D.; Van Speybroeck, V.; Waroquier, M. Global DFT-Based Reactivity Indicators: An Assessment of Theoretical Procedures in Zeolite Catalysis. *J. Phys. Chem. C* **2007**, *111*, 3028−3037.

(32) Chiu, C.; Vayssilov, G. N.; Genest, A.; Borgna, A.; Rösch, N. Predicting adsorption enthalpies on silicalite and HZSM-5: A benchmark study on DFT strategies addressing dispersion interactions. *J. Comput. Chem.* **2014**, *35*, 809−819.

(33) Fischer, M.; Evers, F. O.; Formalik, F.; Olejniczak, A. Benchmarking DFT-GGA calculations for the structure optimisation of neutral-framework zeotypes. *Theor. Chem. Acc.* **2016**, *135*, 257.

(34) Goncalves, T. J.; Plessow, P. N.; Studt, F. On the Accuracy of Density Functional Theory in Zeolite Catalysis. *ChemCatChem* **2019**, *11*, 4368−4376.

(35) Plessow, P. N.; Studt, F. How Accurately Do Approximate Density Functionals Predict Trends in Acidic Zeolite Catalysis? *J. Phys. Chem. Lett.* **2020**, *11*, 4305−4310.

(36) Iron, M. A.; Janes, T. Evaluating Transition Metal Barrier Heights with the Latest Density Functional Theory Exchange−Correlation Functionals: The MOBH35 Benchmark Database. *J. Phys. Chem. A* **2019**, *123*, 3761−3781.

(37) Ruffley, J. P.; Goodenough, I.; Luo, T.-Y.; Richard, M.; Borguet, E.; Rosi, N. L.; Johnson, J. K. Design, Synthesis, and Characterization of Metal−Organic Frameworks for Enhanced Sorption of Chemical Warfare Agent Simulants. *J. Phys. Chem. C* **2019**, *123*, 19748−19758.

(38) Shao, H.; Pandharkar, R.; Cramer, C. J. Factors Affecting the Mechanism of 1,3-Butadiene Polymerization at Open Metal Sites in Co-MFU-4l. *Organometallics* **2022**, *41*, 169−177.

(39) Dohrmann, N.; King, D. S.; Gaggioli, C. A.; Gagliardi, L. Challenge of Small Energy Differences in Metal−Organic Framework Reactivity. *J. Phys. Chem. C* **2023**, *127*, 16891−16900.

(40) Bartlett, R. J.; Stanton, J. F. *Reviews in Computational Chemistry*; John Wiley & Sons, Ltd, 1994; pp 65−169.

(41) Pople, J. A.; Head-Gordon, M.; Raghavachari, K. Quadratic configuration interaction. A general technique for determining electron correlation energies. *J. Chem. Phys.* **1987**, *87*, 5968−5975.

(42) Stanton, J. F. Why CCSD(T) works: a different perspective. *Chem. Phys. Lett.* **1997**, *281*, 130−134.

(43) Fang, Z.; Vasiliu, M.; Peterson, K. A.; Dixon, D. A. Prediction of Bond Dissociation Energies/Heats of Formation for Diatomic Transition Metal Compounds: CCSD(T) Works. *J. Chem. Theory Comput.* **2017**, *13*, 1057−1066.

(44) Karton, A. A computational chemist's guide to accurate thermochemistry for organic molecules. *Wiley Interdiscip. Rev.: Comput. Mol. Sci.* **2016**, *6*, 292−310.

(45) Chan, B.; Ho, J. Simple Composite Approach to Efficiently Estimate Basis Set Limit CCSD(T) Harmonic Frequencies and Reaction Thermochemistry. *J. Phys. Chem. A* **2023**, *127*, 10026−10031.

(46) Guo, Y.; Riplinger, C.; Becker, U.; Liakos, D. G.; Minenkov, Y.; Cavallo, L.; Neese, F. Communication: An improved linear scaling perturbative triples correction for the domain based local pair-natural orbital based singles and doubles coupled cluster method [DLPNO-CCSD(T)]. *J. Chem. Phys.* **2018**, *148*, 011101.

(47) Altun, A.; Riplinger, C.; Neese, F.; Bistoni, G. Exploring the Accuracy Limits of PNO-Based Local Coupled-Cluster Calculations for Transition-Metal Complexes. *J. Chem. Theory Comput.* **2023**, *19*, 2039−2047.

(48) Mallick, S.; Roy, B.; Kumar, P. A comparison of DLPNO-CCSD(T) and CCSD(T) method for the determination of the energetics of hydrogen atom transfer reactions. *Comput. Theor. Chem.* **2020**, *1187*, 112934.

(49) Sauer, J. Ab Initio Calculations for Molecule−Surface Interactions with Chemical Accuracy. *Acc. Chem. Res.* **2019**, *52*, 3502−3510.

(50) Svelle, S.; Tuma, C.; Rozanska, X.; Kerber, T.; Sauer, J. Quantum Chemical Modeling of Zeolite-Catalyzed Methylation Reactions: Toward Chemical Accuracy for Barriers. *J. Am. Chem. Soc.* **2009**, *131*, 816−825.

(51) Hansen, N.; Kerber, T.; Sauer, J.; Bell, A. T.; Keil, F. J. Quantum Chemical Modeling of Benzene Ethylation over H-ZSM-5 Approaching Chemical Accuracy: A Hybrid MP2:DFT Study. *J. Am. Chem. Soc.* **2010**, *132*, 11525−11538.

(52) Gomes, J.; Zimmerman, P. M.; Head-Gordon, M.; Bell, A. T. Accurate Prediction of Hydrocarbon Interactions with Zeolites Utilizing Improved Exchange-Correlation Functionals and QM/MM Methods: Benchmark Calculations of Adsorption Enthalpies and Application to Ethene Methylation by Methanol. *J. Phys. Chem. C* **2012**, *116*, 15406−15414.

(53) Plessow, P. N.; Studt, F. Unraveling the Mechanism of the Initiation Reaction of the Methanol to Olefins Process Using ab Initio and DFT Calculations. *ACS Catal.* **2017**, *7*, 7987−7994.

(54) Yan, Z.; Zhao, T.; Ren, Q. Q. M. QM studies on the mechanisms of interaction of alkenes with zeolitic Brønsted sites in H-FER. *Chem. Phys.* **2024**, *577*, 112136.

(55) Enss, A. E.; Plessow, P. N.; Studt, F. Theoretical investigation of the paring mechanism of the MTO process in different zeolites. *J. Catal.* **2024**, *432*, 115363.

(56) Berger, F.; Rybicki, M.; Sauer, J. Adsorption and cracking of propane by zeolites of different pore size. *J. Catal.* **2021**, *395*, 117−128.

(57) Perdew, J. P.; Burke, K.; Ernzerhof, M. Generalized Gradient Approximation Made Simple. *Phys. Rev. Lett.* **1996**, *77*, 3865−3868.

(58) Tao, J.; Perdew, J. P.; Staroverov, V. N.; Scuseria, G. E. Climbing the Density Functional Ladder: Nonempirical Meta−Generalized Gradient Approximation Designed for Molecules and Solids. *Phys. Rev. Lett.* **2003**, *91*, 146401.

(59) Zhao, Y.; Truhlar, D. G. A new local density functional for main-group thermochemistry, transition metal bonding, thermochemical kinetics, and noncovalent interactions. *J. Chem. Phys.* **2006**, *125*, 194101.

(60) Perdew, J. P.; Tao, J.; Staroverov, V. N.; Scuseria, G. E. Meta-generalized gradient approximation: Explanation of a realistic nonempirical density functional. *J. Chem. Phys.* **2004**, *120*, 6898−6911.

(61) Adamo, C.; Barone, V. Toward reliable density functional methods without adjustable parameters: The PBE0 model. *J. Chem. Phys.* **1999**, *110*, 6158−6170.

(62) Mardirossian, N.; Head-Gordon, M. Survival of the most transferable at the top of Jacob's ladder: Defining and testing the ωB97M(2) double hybrid density functional. *J. Chem. Phys.* **2018**, *148*, 241736.

(63) Zhao, Y.; Truhlar, D. G. The M06 suite of density functionals for main group thermochemistry, thermochemical kinetics, non-covalent interactions, excited states, and transition elements: two new functionals and systematic testing of four M06-class functionals and 12 other functionals. *Theor. Chem. Acc.* **2008**, *120*, 215−241.

(64) Becke, A. D. A new mixing of Hartree−Fock and local density-functional theories. *J. Chem. Phys.* **1993**, *98*, 1372−1377.

(65) Zhao, Y.; Chen, F. Empirical likelihood inference for censored median regression model via nonparametric kernel estimation. *J. Multivar. Anal.* **2008**, *99*, 215−231.

(66) Becke, A. D. Density-functional thermochemistry. I. The effect of the exchange-only gradient correction. *J. Chem. Phys.* **1992**, *96*, 2155−2160.

(67) Planas, N.; Mondloch, J. E.; Tussupbayev, S.; Borycz, J.; Gagliardi, L.; Hupp, J. T.; Farha, O. K.; Cramer, C. J. Defining the Proton Topology of the Zr_6-Based Metal−Organic Framework NU-1000. *J. Phys. Chem. Lett.* **2014**, *5*, 3716−3723.

(68) Grimme, S.; Antony, J.; Ehrlich, S.; Krieg, H. A consistent and accurateab initioparametrization of density functional dispersion correction (DFT-D) for the 94 elements H-Pu. *J. Chem. Phys.* **2010**, *132*, 154104.

(69) Grimme, S.; Ehrlich, S.; Goerigk, L. Effect of the damping function in dispersion corrected density functional theory. *J. Comput. Chem.* **2011**, *32*, 1456−1465.

(70) Kresse, G.; Hafner, J. Ab initio molecular dynamics for liquid metals. *Phys. Rev. B* **1993**, *47*, 558−561.

(71) Kresse, G.; Hafner, J. Ab initio molecular-dynamics simulation of the liquid-metal−amorphous-semiconductor transition in germanium. *Phys. Rev. B* **1994**, *49*, 14251−14269.

(72) Kresse, G.; Furthmüller, J. Efficiency of ab-initio total energy calculations for metals and semiconductors using a plane-wave basis set. *Comput. Mater. Sci.* **1996**, *6*, 15−50.

(73) Kresse, G.; Furthmüller, J. Efficient iterative schemes for ab initio total-energy calculations using a plane-wave basis set. *Phys. Rev. B* **1996**, *54*, 11169−11186.

(74) Neese, F. Software update: The ORCA program system—Version 5.0. *Wiley Interdiscip. Rev.: Comput. Mol. Sci.* **2022**, *12*, No. e1606.

(75) Weigend, F.; Ahlrichs, R. Balanced basis sets of split valence, triple zeta valence and quadruple zeta valence quality for H to Rn: Design and assessment of accuracy. *Phys. Chem. Chem. Phys.* **2005**, *7*, 3297.

(76) Neese, F.; Hansen, A.; Liakos, D. G. Efficient and accurate approximations to the local coupled cluster singles doubles method using a truncated pair natural orbital basis. *J. Chem. Phys.* **2009**, *131*, 064103.

(77) Brogaard, R. Y.; Kømurcu, M.; Dyballa, M. M.; Botan, A.; Van Speybroeck, V.; Olsbye, U.; De Wispelaere, K. Ethene Dimerization on Zeolite-Hosted Ni Ions: Reversible Mobilization of the Active Site. *ACS Catal.* **2019**, *9*, 5645−5650.

(78) Kozuch, S.; Shaik, S. How to Conceptualize Catalytic Cycles? The Energetic Span Model. *Acc. Chem. Res.* **2011**, *44*, 101−110.

(79) Bernales, V.; Ortuño, M. A.; Truhlar, D. G.; Cramer, C. J.; Gagliardi, L. Computational Design of Functionalized Metal−Organic Framework Nodes for Catalysis. *ACS Cent. Sci.* **2018**, *4*, 5−19.

(80) Mancuso, J. L.; Mroz, A. M.; Le, K. N.; Hendon, C. H. Electronic Structure Modeling of Metal−Organic Frameworks. *Chem. Rev.* **2020**, *120*, 8641−8715.

(81) Benali, A.; Luo, Y.; Shin, H.; Pahls, D.; Heinonen, O. Quantum Monte Carlo Calculations of Catalytic Energy Barriers in a Metallorganic Framework with Transition-Metal-Functionalized Nodes. *J. Phys. Chem. C* **2018**, *122*, 16683−16691.

(82) Yang, D.; Odoh, S. O.; Wang, T. C.; Farha, O. K.; Hupp, J. T.; Cramer, C. J.; Gagliardi, L.; Gates, B. C. Metal−Organic Framework Nodes as Nearly Ideal Supports for Molecular Catalysts: NU-1000- and UiO-66-Supported Iridium Complexes. *J. Am. Chem. Soc.* **2015**, *137*, 7391−7396.

(83) Yang, D.; Odoh, S. O.; Borycz, J.; Wang, T. C.; Farha, O. K.; Hupp, J. T.; Cramer, C. J.; Gagliardi, L.; Gates, B. C. Tuning Zr_6 Metal−Organic Framework (MOF) Nodes as Catalyst Supports: Site Densities and Electron-Donor Properties Influence Molecular Iridium Complexes as Ethylene Conversion Catalysts. *ACS Catal.* **2016**, *6*, 235−247.

(84) Ortuño, M. A.; Bernales, V.; Gagliardi, L.; Cramer, C. J. Computational Study of First-Row Transition Metals Supported on MOF NU-1000 for Catalytic Acceptorless Alcohol Dehydrogenation. *J. Phys. Chem. C* **2016**, *120*, 24697−24705.

(85) Yang, D.; Momeni, M. R.; Demir, H.; Pahls, D. R.; Rimoldi, M.; Wang, T. C.; Farha, O. K.; Hupp, J. T.; Cramer, C. J.; Gates, B. C.; Gagliardi, L. Tuning the properties of metal−organic framework nodes as supports of single-site iridium catalysts: node modification by atomic layer deposition of aluminium. *Faraday Discuss.* **2017**, *201*, 195−206.